Nur'ainul Miftahul Huda

Gita

Paper 4
FMIPA Oke
Universitas Tanjungpura

Document Details

Submission ID
trn:oid:::1:3407406702

Submission Date
Nov 12, 2025, 9:23 AM GMT+7

Download Date
Nov 12, 2025, 9:33 AM GMT+7

File Name
Cauchy_Gita_8_.pdf

File Size
4.2 MB

16 Pages

7,597 Words

39,420 Characters

10% Overall Similarity

The combined total of all matches, including overlapping sources, for each database.

Filtered from the Report

- Bibliography
- Quoted Text

Match Groups

45 Not Cited or Quoted 9%
Matches with neither in-text citation nor quotation marks

4 Missing Quotations 1%
Matches that are still very similar to source material

0 Missing Citation 0%
Matches that have quotation marks, but no in-text citation

0 Cited and Quoted 0%
Matches with in-text citation present, but no quotation marks

Top Sources

7% Internet sources
9% Publications
3% Submitted works (Student Papers)

Match Groups

- **45** Not Cited or Quoted 9%
  Matches with neither in-text citation nor quotation marks
- **4** Missing Quotations 1%
  Matches that are still very similar to source material
- **0** Missing Citation 0%
  Matches that have quotation marks, but no in-text citation
- **0** Cited and Quoted 0%
  Matches with in-text citation present, but no quotation marks

Top Sources

- 7% Internet sources
- 9% Publications
- 3% Submitted works (Student Papers)

Top Sources

The sources with the highest number of matches within the submission. Overlapping sources will not be displayed.

1	Internet	journal.ummat.ac.id 2%
2	Internet	ojs3.unpatti.ac.id 1%
3	Internet	ejournal.uin-malang.ac.id <1%
4	Publication	Manoranjan Mishra, Rajkumar Guria, Biswaranjan Baraj, Celso Augusto Guimarã... <1%
5	Publication	Nur'ainul Miftahul Huda, Nurfitri Imro'ah, Muhammad Yahya Ayyash, Hesty Prati... <1%
6	Student papers	School of Business and Management ITB <1%
7	Student papers	University of Durham <1%
8	Publication	Fitri Amalia, Achmad Fauzan. "ESTIMATING EARTHQUAKE MAGNITUDE USING SPA... <1%
9	Internet	www.preprints.org <1%
10	Internet	hal.science <1%

11 Student papers
Monash University <1%

12 Publication
Hesty Pratiwi, Nurfitri Imro'ah, Nur'ainul Miftahul Huda. "FOREST FIRE ANALYSIS ... <1%

13 Publication
Haiyang Xia, Song Zha, Jijun Huang, Jibin Liu. "Radio environment map constructi... <1%

14 Internet
bioone.org <1%

15 Internet
www.intechopen.com <1%

16 Publication
Muhammad Yahya Ayyash, Nur'ainul Miftahul Huda, Nurfitri Imro'ah. "The GSTA... <1%

17 Publication
Utriweni Mukhaiyar, Bayu Imadul Bilad, Udjianna Sekteria Pasaribu. "The Genera... <1%

18 Internet
www.researchsquare.com <1%

19 Publication
S. Reza H. Shojaei, Yadollah Waghei, Mohsen Mohammadzadeh. "Geostatistical a... <1%

20 Publication
Utriweni Mukhaiyar, Adilan Widyawan Mahdiyasa, Tarasinta Prastoro, Udjianna S... <1%

21 Internet
roderic.uv.es <1%

22 Publication
Elizabeth B. Wiggins, Amber J. Soja, Emily Gargulinski, Hannah S. Halliday et al. "H... <1%

23 Internet
pure.tue.nl <1%

24 Internet
www.mdpi.com <1%

CAUCHY – Jurnal Matematika Murni dan Aplikasi
Volume 10 (2) (2025), Pages 427-442
p-ISSN: 2086-0382; e-ISSN: 2477-3344

Interpolation of Fire Radiative Power Based on GSTAR Model Predictions with Queen Contiguity Weights Using Ordinary Kriging

Gita Fitriyana[1], Nurfitri Imro'ah[1*], and Nur'ainul Miftahul Huda[2]

[1]*Department of Statistics, Universitas Tanjungpura, Indonesia*
[2]*Department of Mathematics, Universitas Tanjungpura, Indonesia*

Abstract

Forest fires are a persistent environmental issue in West Kalimantan, Indonesia, driven by both natural and human factors. Fire Radiative Power (FRP) serves as a vital indicator for assessing wildfire intensity and energy release. This study aims to model and predict the spatial temporal dynamics of FRP using the Generalized Space Time Autoregressive [GSTAR(1;1)] model combined with Ordinary Kriging interpolation. The dataset covers West Kalimantan from July 2024 to September 2025, comprising four attributes: observation date, longitude, latitude, and FRP value. Data filtering was applied from the national to provincial level, focusing on three regencies Sanggau, Sekadau, and Ketapang across 14 sub-districts represented by a 1.25×1.25 grid. The data consisted of 65 weekly observations, with 61 used for training and 4 for testing. The GSTAR(1,1) model with a spatial area-based framework achieved an optimal MAPE of 12.63% and satisfied the white noise assumption, indicating reliable performance. Predictions for October 2025 indicated relatively stable fire intensity, with a slight FRP decrease in Nanga Tayap and Sandai during the final week. Overall, the integrated GSTAR–Kriging framework effectively captured both temporal and spatial variations, supporting improved fire risk assessment and regional decision making for wildfire management in West Kalimantan.

Keywords: Weight; Spatial Temporal; Kriging; Forest Fire

1 Introduction

Fire Radiative Power (FRP) serves as a fundamental indicator for characterising fire behaviour, as it reflects the rate at which heat energy is released during combustion [1]. In addition, FRP functions as an important parameter for assessing wildfire intensity, providing more detailed quantitative information than conventional fire perimeter or burned area datasets that typically offer only binary classifications [2]. Furthermore, FRP represents a valuable quantitative indicator of fire activity and its temporal variations over the study period [3]. Over the past two decades, numerous operational remote sensing approaches have been developed and widely implemented to estimate FRP, enabling the evaluation of combustion intensity and emission levels [4]. Therefore, accurate prediction of FRP is essential not only for improving the effectiveness of wildfire

*Corresponding author. E-mail: nurfitriimroah@math.untan.ac.id

Submitted: ... Reviewed: ... Accepted: ...
DOI: https://doi.org/10.18860/cauchy.v10i2.32446

management and suppression strategies but also for assessing the environmental pollution impacts arising from such events [5].

Forest fires are among the most frequent environmental disasters in Indonesia, particularly in the province of West Kalimantan. These events are driven by a combination of natural factors, such as prolonged droughts and the El Niño phenomenon, alongside human activities like land clearing through burning practices [6]. Additionally, forest fires also referred to as bushfires or vegetation fires can be triggered by climatic shifts that are further intensified by increasing greenhouse gas emissions and global warming [7]. In fact, more than 90% of forest fires are attributed to human activities, while the remaining cases are primarily caused by natural phenomena such as lightning strikes [8]. In this study, the analysis focuses on three regencies: Sanggau, Sekadau, and Ketapang, which collectively represent the primary hotspot corridor in West Kalimantan (see Figure 1). Figure 1b classifies the regencies based on their total accumulated FRP, with colors indicating the ranking: Red (highest), Pink (moderate), and Yellow (lower). Ketapang (319.1 MW) and Sanggau (279.2 MW) record the highest peak FRP intensities, whereas Sekadau (199.0 MW), despite a lower maximum value, was included because it geographically connects the two major hotspot regions. These three regencies thus form a spatially contiguous zone of intense fire activity extending from the central region to the southern coast, making them suitable for spatial temporal interaction analysis.

(a) **(b)**

Figure 1: Spatial distribution of FRP in (a) West Kalimantan and (b) the selected study area comprising Sanggau, Sekadau, and Ketapang regencies.

To analyze the spatial and temporal dynamics of fire activity in the study area, this research employs the Generalized Space–Time Autoregressive (GSTAR) model with a spatial weight matrix based on the Queen contiguity criterion. The GSTAR(1;1) specification is particularly suitable for modelling the interdependence of fire behaviour across neighbouring regions over time, allowing the identification of spatial autocorrelation and temporal persistence in FRP values, since the GSTAR model explains the manner in which patterns of change and interactions occur between locations within a spatial-temporal system [9]. By incorporating both spatial and temporal components, this model can effectively capture the propagation patterns of fire activity between adjacent grid areas [10]. The best-performing GSTAR model is then used to generate FRP predictions, which are subsequently interpolated using the Ordinary Kriging technique. This method is recognised as the most effective linear and unbiased interpolation for estimating unknown spatial values [11] and provides a geostatistical framework for estimating FRP intensity at unsampled locations and enhancing spatial continuity. The integration of GSTAR and Ordinary Kriging enables a comprehensive spatial-temporal assessment, revealing not only how fire activity evolves over time but also how it spreads spatially across West Kalimantan.

Several previous studies have explored FRP prediction using spatial approaches. A study combining the GSTAR and Ordinary Kriging models analyzed CO_2 emission variability in Asia, identifying China, India, and Indonesia as the largest contributors. The $GSTAR(3;1,1,1)$ model provided optimal forecasts with low RMSE and MAPE values, while the isotropic spherical semivariogram in Kriging produced accurate spatial predictions, indicating persistently high

emissions in northeastern Asia until 2027 [12]. Another study utilizing FRP data from MODIS satellites across countries such as Nepal, Bhutan, and Sri Lanka applied spatial statistical methods including the Spatial Lag Model, Spatial Error Model, and Kriging to map and predict FRP distribution. Kriging interpolation was used to estimate fire potential in unobserved areas, offering a comprehensive overview of fire risk and impact [13]. Additionally, a study on peatland fires in Kubu Raya Regency, West Kalimantan, analyzed fire dynamics using temporal, spatial, and spatial temporal approaches. The ARIMA model captured temporal trends, Kriging interpolation mapped spatial hotspot distribution, and the GSTAR model identified areas with a high potential for future fire spread [14].

This study aims to model and predict the spatial-temporal dynamics of FRP across 14 selected sub-districts within the regencies of Sanggau, Sekadau, and Ketapang in West Kalimantan Province using the GSTAR model combined with the Ordinary Kriging method. The main objective is to capture both the spatial interaction and temporal persistence of fire activity, enabling a more detailed understanding of fire propagation patterns within the study area. By integrating FRP with geostatistical and spatial-temporal modelling techniques, this research aims to produce accurate and continuous predictions of fire intensity distribution. The novelty of this study lies in combining GSTAR for temporal forecasting and Ordinary Kriging for spatial interpolation, providing a robust framework to improve fire risk assessment and support regional decision-making for wildfire management and environmental protection in West Kalimantan.

2 Methods

This study adopts a quantitative research approach that integrates spatial and temporal analysis through the GSTAR model. The objective is to analyse and model the spatial-temporal dynamics of FRP across selected sub-districts in Sanggau, Sekadau, and Ketapang Regencies, West Kalimantan. The best GSTAR model results are further refined using the Ordinary Kriging method to generate spatially continuous predictions of fire intensity.

2.1 Generalized Space-Time Autoregressive Model (GSTAR)

The Generalized Space-Time Autoregressive (GSTAR) model is commonly applied in conducting spatio-temporal analysis [15]. The autoregressive (AR) model served as the foundation for the development of the space-time autoregressive (STAR) model, which later evolved into the generalized spatio-temporal autoregressive (GSTAR) model that extends its predecessors by incorporating both spatial interactions among locations and temporal variations over time [6], [16]. The GSTAR model can be represented as follows.

$$\mathbf{Y}_t = \sum_{s=1}^{p} \left[\mathbf{\Phi}_{s0} + \sum_{k=1}^{\lambda_s} \mathbf{\Phi}_{sk} \mathbf{W}_k \right] \mathbf{Y}_{t-k} + \mathbf{e}_t \tag{1}$$

where $\mathbf{W}_k$ is weight matrix. Assuming that $\mathbf{Y}_t$ follows the GSTAR(1;1) model, then:

$$\mathbf{Y}_t = \mathbf{\Phi}_{10}\mathbf{W}^{(0)}\mathbf{Y}_{t-1} + \mathbf{\Phi}_{11}\mathbf{W}^{(1)}\mathbf{Y}_{t-1} + \mathbf{e}_t \tag{2}$$

where,

$$\mathbf{Y}_t = \begin{bmatrix} Y_t^{(1)} & Y_t^{(2)} & \dots & Y_t^{(N)} \end{bmatrix}^t$$
$$\mathbf{\Phi}_{10} = \text{diag}(\phi_{10}^{(1)}, \phi_{10}^{(2)}, \dots, \phi_{10}^{(N)})$$
$$\mathbf{\Phi}_{11} = \text{diag}(\phi_{11}^{(1)}, \phi_{11}^{(2)}, \dots, \phi_{11}^{(N)})$$
$$\mathbf{e}_t = \begin{bmatrix} e_t^{(1)} & e_t^{(2)} & \dots & e_t^{(N)} \end{bmatrix}^t$$

The variables in the model are defined as follows: $\mathbf{Y}_t$ is observations in period t, while $\mathbf{Y}_{t-1}$ is observations in the preceding period, $t-1$. The parameter $\mathbf{\Phi}_{10}$ is the autoregressive coefficient for the influence of the location itself, whereas $\mathbf{\Phi}_{11}$ is the autoregressive coefficient for the influence of neighboring locations. Furthermore, $\mathbf{W}^{(0)}$ is an identity matrix, $\mathbf{W}^{(1)}$ is the spatial weight matrix, and $\mathbf{e}_t$ is the error term in period t. Equation 2 can alternatively be expressed as follows for the GSTAR(1;1) model:

2.2 Queen Contiguity Weight Matrix

The spatial weight matrix plays a crucial role in constructing the GSTAR model, as it helps represent the spatial relationships among different locations [17]. It also serves as a fundamental element in spatial analysis, providing a means to evaluate the interactions and dependencies that occur among geographic areas [18]. A spatial weight matrix can be built in several ways, one of which is the queen contiguity method. In this method, the weight of each location is based on nearby areas that share common boundaries or corner points [16]. The spatial weight matrix must satisfy specific conditions. A primary requirement is that a location has no spatial influence on itself, meaning the diagonal elements of the matrix are zero ($w_{ij} = 0$ for $i = j$, where $i = 1, 2, \ldots, N$). Therefore, the general form of the $N \times N$ weight matrix, denoted as $\mathbf{W}$, can be represented as follows [19]:

$$\mathbf{W}^{(\ell)} = \begin{bmatrix} 0 & w_{12}^{(\ell)} & \ldots & w_{1N}^{(\ell)} \\ w_{21}^{(\ell)} & 0 & \ldots & w_{2N}^{(\ell)} \\ \vdots & \vdots & \ddots & \vdots \\ w_{N1}^{(\ell)} & w_{N2}^{(\ell)} & \ldots & 0 \end{bmatrix} \tag{3}$$

where $\mathbf{W}^{(\ell)}$ represents the spatial weight matrix at spatial lag ℓ.

2.3 Ordinary Kriging

Kriging is a geostatistical technique used to perform spatial interpolation [20]. It encompasses a set of interpolation methods grounded in geostatistics that aim to provide unbiased estimates of variable values across a surface [21]. In general, various types of kriging methods are available, including ordinary, simple, universal, Poisson probability, and others [22]. Among these, Ordinary Kriging is recognized as an effective and efficient approach for interpolating sparse geospatial data across extensive areas [20]. This method utilizes spatial data from sampled points along with variograms that describe the correlation between spatial locations to estimate values at unsampled sites, where the predicted values are influenced by their proximity to the sampled locations [23]. This method assumes that the study variable at any given location is a stationary random function, meaning that its mean value remains constant throughout the study area, although the exact value of the mean is unknown [24]. The equation of the Ordinary Kriging model is expressed as follows [25].

$$\hat{Z}(u_0) = \sum_{i=1}^{n} w_i Z(u_0) \tag{4}$$

where the value at an unobserved location, u_0, is estimated and denoted by $\hat{Z}(u_0)$. This estimate is calculated as a weighted average of the observed values, $Z(u_i)$, from n surrounding data points at locations u_i. Each of these observations is assigned a specific weight, w_i, which is determined by the distance and spatial relationship between the points. One of the main objectives of the Kriging method is to obtain an optimal, linear, and unbiased estimate (BLUE) [26].

2.4 Variogram and Semivariogram

The variogram is a key instrument in geostatistics that illustrates the spatial autocorrelation and measurement variability among the data points being analyzed [20], and it plays a crucial role in determining the weighting factors used for interpolation in the Kriging process [24]. The estimated experimental variogram can be expressed as follows [23]:

$$2\hat{\gamma}(h) \equiv \frac{1}{|N(h)|} \sum_{N(h)} [z(s_i) - z(s_j)]^2 \tag{5}$$

where $z(s_i)$ and $z(s_j)$ are field values at locations s_i and s_j, respectively. The set of all location pairs separated by the lag distance $\mathbf{h}$ is denoted by $N(h) = \{(s_i, s_j) : s_i - s_j \in h$ for $i, j = 1, \ldots, N\}$, whereas $|N(h)|$ denotes the number of distinct pairs in $N(h)$.

The semivariogram is defined as one-half of the variogram value [2]. In general, semivariograms are categorized into two types: the empirical semivariogram and the theoretical semivariogram [23]. The experimental semivariogram represents a plot of semivariance values $\gamma(h)$ as a function of the separation distance h [27]. The experimental semivariogram is derived from observed or sampled data using the following equation [28].

$$\hat{\gamma}(h) \equiv \frac{1}{2|N(h)|} \sum_{N(h)} [z(s_i) - z(s_j)]^2 \tag{6}$$

The experimental semivariogram values are subsequently compared with theoretical models to determine the best-fitting one, which is then used in calculating the weights for the Kriging interpolation process. In general, theoretical semivariograms are classified into three main types: Spherical, Exponential, and Gaussian [29].

The research workflow is presented in Figure 2, outlining the sequential procedures carried out in this study from data acquisition and preprocessing to model development, validation, and spatial interpolation using the GSTAR–Kriging approach.

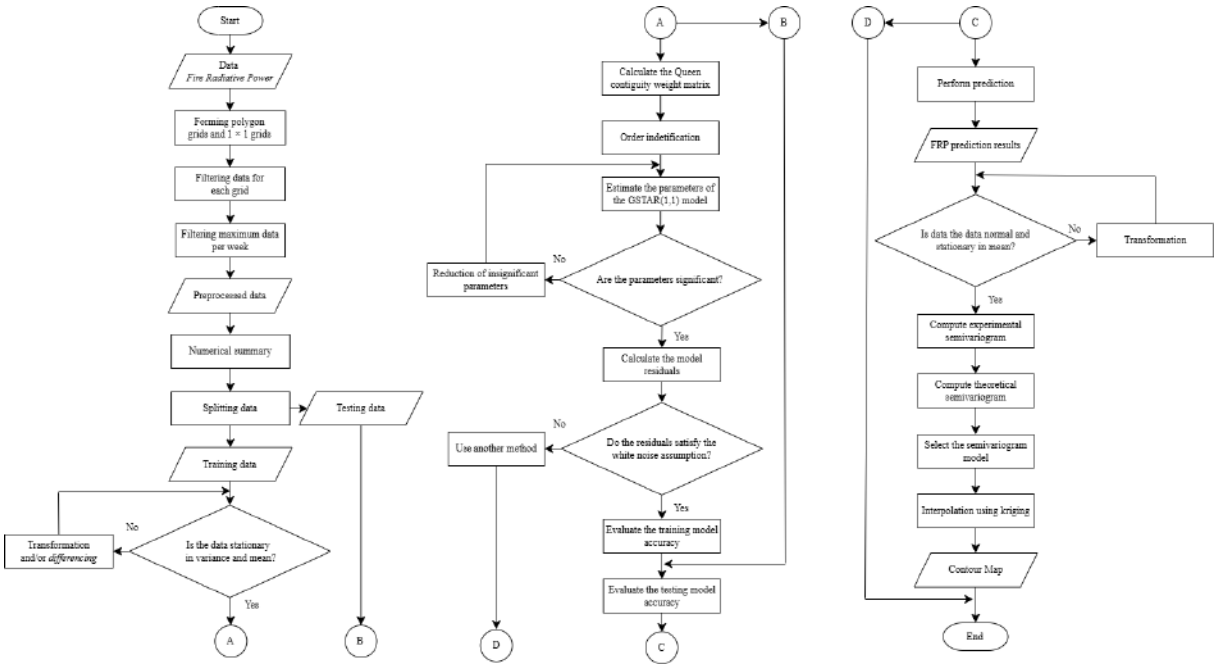

Figure 2: Research flowchart

3 Results and Discussion

The data used in this study comprise Fire Radiative Power (FRP) values obtained from the VIIRS NOAA-20 satellite through the official NASA FIRMS platform. FRP represents the

rate of radiant energy released by active fires, expressed in megawatts (MW), and serves as an indicator of fire intensity and combustion efficiency. An illustration of the FRP data distribution can be seen in Figure 3 [30].

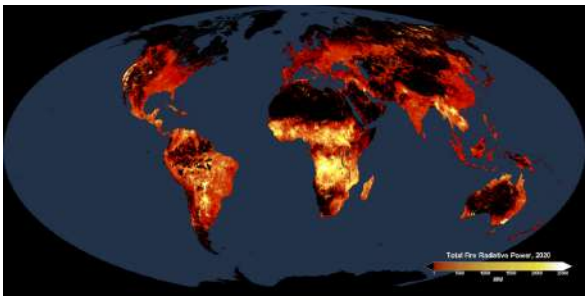

Figure 3: Ilustration of Fire Radiative Power

The dataset covers West Kalimantan Province over the period from July 2024 to September 2025 and includes four key attributes: observation date, longitude, latitude, and FRP value. The initial stage of data processing involved applying a geographical filter, starting from the national scale (covering all of Indonesia), which was then narrowed to Kalimantan Island and further refined to West Kalimantan Province specifically focusing on three regencies: Sanggau, Sekadau, and Ketapang. From these regencies, 14 sub-districts were selected as the spatial units of analysis (see Figure 4a).

Subsequently, the 14 sub-districts were transformed into spatial representations using 1.25×1.25 grid, resulting in three research zones labeled A1, A2, and A3 (see Figure 4b). Following the spatial transformation, data preprocessing was carried out to ensure the dataset met the assumptions required for model development. The FRP data were aggregated into 65 weekly observations, with each observation representing the maximum FRP value recorded during that week for each grid area. From this dataset, 61 observations (July 2024–August 2025) were used as the training set, while the remaining 4 observations (September 2025) served as the testing set. The trained model was then used to generate predictions for October 2025.

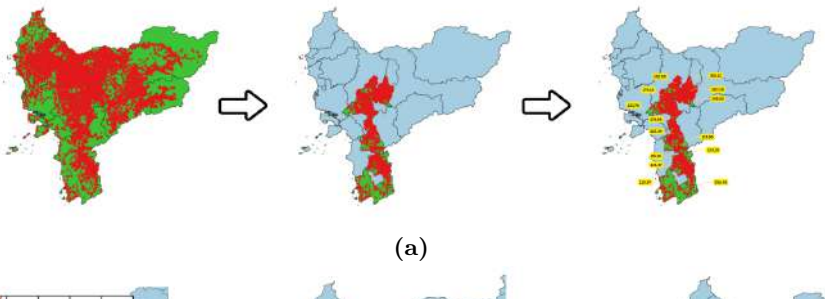

(a)

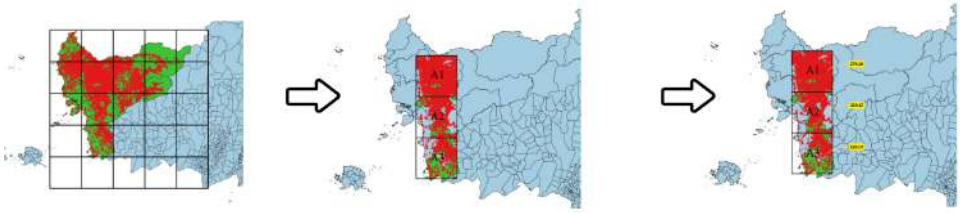

(b)

Figure 4: Illustration of the data preprocessing process for (a) spatial area-based and (b) 1.25×1.25 grid cells.

To visually examine the temporal dynamics and characteristics of the prepared data, time series plot of the weekly maximum FRP values are presented in Figure 5. The figure illustrates the data from two perspectives: the aggregated grid locations that serve as the direct input for the GSTAR model, and the original administrative sub-districts, which provide contextual

comparison.

A visual examination of the plots reveals a distinct seasonal pattern in fire activity across the study area. The time series at both the district level (see Figure 5a) and the grid-based representation (see Figure 5b) exhibit two prominent peaks, occurring approximately around weeks 11–13 and week 56, which coincide with the dry season when fires are most prevalent. In Figure 5a, only a subset of representative districts three selected areas is displayed to illustrate the general temporal trend observed across all regions. After spatial aggregation into grid form, this temporal pattern remains evident and demonstrates strong synchronization among locations, indicating the presence of spatial dependence in fire occurrences, which provides the key rationale for applying the GSTAR model.

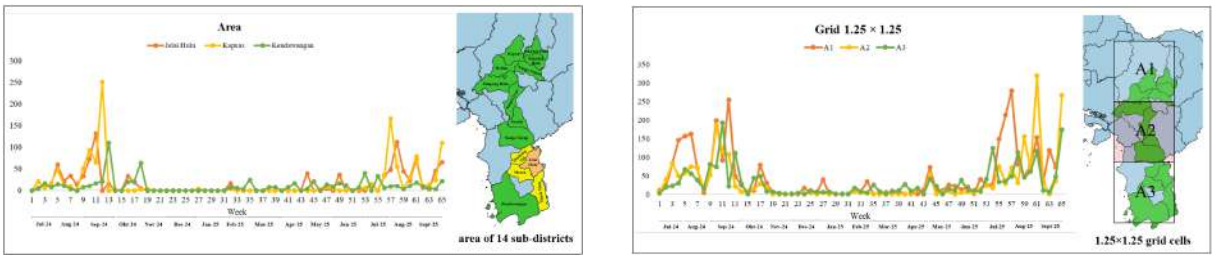

(a) **(b)**

Figure 5: FRP data plot and ilustration of Queen Contiguity weight for (a) spatial area-based and (b) 1.25×1.25 grid cells.

While these plots effectively illustrate the temporal dynamics and spatial co-movement of fire activity, a more formal quantitative summary is necessary to compare the statistical characteristics of each location accurately. Therefore, a descriptive statistical analysis was conducted, and the results are summarized in Table 1.

Table 1: Statistical summary. The bolded numbers represents the maximum values.

Spatial Unit	Locations (i)	Maximum	Minimum	Mean	Std. Deviation
Area	Jelai Hulu (1)	133.18	0.51	16.22	27.73
	Kapuas (2)	252.09	2.66	18.05	42.37
	Kendawangan (3)	110.97	3.86	10.55	16.98
	Manis Mata (4)	193.07	2.33	10.21	26.81
	Marau (5)	173.68	1.16	14.17	31.67
	Meliau (6)	279.19	3.28	**25.41**	**49.03**
	Nanga Taman (7)	145.93	3.13	14.32	31.03
	Nanga Tayap (8)	107.59	2.54	10.71	20.79
	Sandai (9)	255.43	3.23	19.01	42.36
	Sekadau Hilir (10)	182.54	3.66	13.37	30.52
	Sekadau Hulu (11)	198.95	2.35	16.13	36.51
	Simpang Hulu (12)	**319.12**	2.31	17.52	47.28
	Sungai Laur (13)	280.29	2.59	17.58	47.13
	Tumbang Titi (14)	82.48	0.91	8.48	16.99
Grid 1.25×1.25	A1 (1)	279.19	0.48	**50.05**	**67.91**
	A2 (2)	**319.12**	2.26	33.89	60.60
	A3 (3)	193.07	2.37	31.18	40.95

Note: All FRP values are expressed in Megawatts (MW).

Based on Table 1, the analysis at the polygon (sub-district) level shows clear variations in fire intensity across regions. The highest maximum FRP values are observed in Simpang Hulu (319.12 MW) and Sungai Laur (280.29 MW), which occurred during week 61, corresponding to August 2025, indicating that the most intense fire events took place in these sub-districts. Regarding the average FRP, Meliau (25.41 MW) records the highest value within the past year, suggesting

that this area consistently experienced elevated fire activity compared to other sub-districts such as Marau (14.17 MW) and Tumbang Titi (8.48 MW). The relatively high standard deviations observed in Meliau (49.03) and Simpang Hulu (47.28) further indicate fluctuating fire intensity patterns characterized by intermittent peaks of extreme fire activity.

When the data are aggregated into the 1.25×1.25 grid system, which serves as the direct input for the GSTAR model, a clearer picture of the broader hotspot zones emerges. A key observation is that Grid A1 exhibits the highest mean FRP value (50.05 MW), substantially exceeding that of Grid A2 (33.89 MW) and Grid A3 (31.18 MW). This indicates that Grid A1 consistently experienced higher fire intensity throughout the past year of observation.

Conversely, the most extreme single event occurred within Grid A2, which recorded a maximum FRP of 319.12 MW. This peak was observed in week 61, corresponding to August 2025, and directly aligns with the highest FRP detected in the Sekadau Hilir sub-district, confirming that this major fire event was geographically located within the A2 grid boundaries. The relatively high standard deviations in Grid A1 (67.91) and Grid A2 (60.60) further reinforce the visual findings from the plots, suggesting that these two grids are not only the most active but also the most volatile areas.

3.1 Stasionarity Test

In constructing the GSTAR model, it is necessary to ensure that the data exhibits stability in both its mean and variance [31]. Furthermore, the Augmented Dickey-Fuller (ADF) test is performed to assess whether the data is stationary with respect to its mean [32]. The results of the ADF test indicate that the data are non-stationary in the mean for both the spatial area-based model and the 1.25×1.25 grid. This is evidenced by ADF values greater than 0.05. Therefore, differencing was applied to both datasets, as presented in Table 2. After differencing, the analysis could proceed to the next stage.

Table 2: ADF Test Results

ADF Test	**Locations (i)**													
	1	**2**	**3**	**4**	**5**	**6**	**7**	**8**	**9**	**10**	**11**	**12**	**13**	**14**
Area	0.01	0.01	0.01	0.01	0.01	0.01	0.01	0.01	0.01	0.01	0.01	0.18	0.04	0.01
Grid 1.25×1.25	0.01	0.04	0.01											

3.2 Queen Contiguity Weight Matrix

The Queen Contiguity rule will be applied in the next step to construct the spatial weight matrix. By implementing this rule on the generated location, two matrices are defined as $\boldsymbol{W}_{Q1}^{(1)}$ for the spatial area-based model and $\boldsymbol{W}_{Q2}^{(1)}$ for the 1.25×1.25 grid, where $\boldsymbol{W}_{Q1}^{(1)}$ denotes the first-order for spatial area-based model.

$$\mathbf{W}_{Q1}^{(1)} = \begin{bmatrix} 0 & 0 & 0 & 0.33 & 0.33 & 0.33 & \cdots & 0.33 \\ 0 & 0 & 0 & 0 & 0 & 0.25 & \cdots & 0 \\ 0 & 0 & 0 & 0.5 & 0.5 & 0 & \cdots & 0 \\ \vdots & \vdots & \vdots & \vdots & \vdots & \vdots & \ddots & \vdots \\ 0.33 & 0 & 0 & 0 & 0.33 & 0 & \cdots & 0 \end{bmatrix} \qquad \mathbf{W}_{Q2}^{(1)} = \begin{bmatrix} 0 & 1 & 1 \\ 0.5 & 0 & 0.5 \\ 0 & 1 & 0 \end{bmatrix}$$

In the spatial area-based, a value of 1 indicates that two sub-districts are adjacent, and 0 otherwise. Based on Figure 5 the sub-district highlighted in cream (Jelai Hulu) represents the observed location, while the yellow areas indicate its first-order neighbours. Likewise, in the 1.25×1.25 grid, the red-hatched cell (A2) denotes the observed location, with A1 and A3

identified as its neighbours. These matrices clearly illustrate the spatial adjacency captured by the first-order Queen Contiguity rule. In the GSTAR(1;1) models, only this first-order spatial lag is considered, as it sufficiently represents the spatial dependencies required for accurate parameter estimation.

3.3 Parameter Estimation and Diagnostic Test

The parameter estimation for the GSTAR(1;1) models was conducted using the Ordinary Least Squares (OLS) method with the previously defined Queen Contiguity spatial weights. Table 3 presents the results of this initial estimation, along with the diagnostic tests for the model residuals. For a model to be considered valid, its residuals must satisfy the white noise assumption, meaning they are both independent and normally distributed.

The parameter estimation results in Table 3 reveal varied values across locations. In the initial estimation (before), several parameters were found to be statistically insignificant, as indicated by the red text. Here, the term before refers to the results of the first parameter estimation, prior to the re-estimation process, while after denotes the results obtained following the re-estimation. An insignificant parameter does not contribute meaningfully to the model's predictive power and must be excluded to create a more parsimonious and robust model. Consequently, a re-estimation process was performed. The insignificant parameters were set to zero (highlighted in blue) and removed, and the model was refitted iteratively until only significant parameters remained. This refinement ensures that the final model is both statistically valid and efficient. The after results, representing the final set of fully significant parameters, are presented in Table 3.

Table 3: Parameter estimation and diagnostic test. Red and blue values represent insignificant parameters and those set to zero, respectively. "Yes" indicates that the normality and independence assumptions are satisfied, while "No" indicates that they are not.

Spatial Unit	Loc. (i)	Before					After				
		Parameter		Diag.Test		MAPE	Parameter		Diag.Test		MAPE
		$\phi_{10}^{(i)}$	$\phi_{11}^{(i)}$	Norm.	Ind.		$\phi_{10}^{(i)}$	$\phi_{11}^{(i)}$	Norm.	Ind.	
Area	Jelai Hulu (1)	-0.02	0.36	Yes	Yes	13.37%	0.00	0.34	Yes	Yes	**12.63%**
	Kapuas (2)	-0.06	-0.36	Yes	Yes		-0.06	-0.36	Yes	Yes	
	Kendawangan (3)	-0.54	0.60	Yes	Yes		-0.54	0.60	Yes	Yes	
	Manis Mata (4)	0.09	-0.10	Yes	Yes		0.07	0.00	Yes	Yes	
	Marau (5)	-0.02	0.01	Yes	Yes		0.00	0.00	Yes	Yes	
	Meliau (6)	0.00	0.00	Yes	Yes		0.00	0.00	Yes	Yes	
	Nanga Taman (7)	-0.03	0.00	Yes	Yes		0.00	0.00	Yes	Yes	
	Nanga Tayap (8)	0.01	-0.01	No	Yes		0.00	0.00	Yes	Yes	
	Sandai (9)	0.00	0.01	Yes	Yes		0.00	0.00	Yes	Yes	
	Sekadau Hilir (10)	-0.02	0.02	No	Yes		0.00	0.00	Yes	Yes	
	Sekadau Hulu (11)	-0.01	-0.02	No	Yes		0.00	0.00	Yes	Yes	
	Simpang Hulu (12)	-0.05	0.12	Yes	Yes		0.00	0.10	Yes	Yes	
	Sungai Laur (13)	-0.02	-0.50	Yes	Yes		0.00	-0.52	Yes	Yes	
	Tumbang Titi (14)	-0.97	-0.76	Yes	Yes		-0.97	-0.76	Yes	Yes	
Grid 1.25×1.25	A1 (1)	-0.02	0.13	Yes	Yes	13.49%	0.00	0.15	Yes	Yes	11.76%
	A2 (2)	-0.04	0.05	Yes	Yes		0.00	0.00	Yes	Yes	
	A3 (3)	-0.24	0.14	Yes	Yes		-0.24	0.14	Yes	No	

For the spatial area-based model, after the re-estimation process, the significant parameters were identified as: ϕ_{11} for Jelai Hulu; both ϕ_{10} and ϕ_{11} for Kapuas and Kendawangan; ϕ_{10} for Manis Mata; ϕ_{11} for Simpang Hulu and Sungai Laur; and both ϕ_{10} and ϕ_{11} for Tumbang Titi. The resulting refined model achieved a significantly improved MAPE of 12.63%, and its residuals successfully met the assumptions of normality and independence. For the Grid 1.25×1.25 model, the re-estimation process yielded a final model where the significant parameters were the spatial parameter (ϕ_{11}) for location A1, and both the temporal (ϕ_{10}) and spatial (ϕ_{11}) parameters for

location A3. Notably, for location A2, both parameters were found to be insignificant and were thus removed from the final model. This refined grid model produced a MAPE of 11.76%, with its residuals satisfying the normality assumption but not the independence assumption.

3.4 Accuracy Model

A comparison of the predictive accuracy between the two final models shows that both the spatial area-based model (MAPE = 12.63%, see the bolded value in Table 3) and the Grid 1.25×1.25 model (MAPE = 11.76%, as shown in the MAPE column of Table 3) demonstrate strong forecasting performance. However, the spatial area-based model was selected as the final model because its residuals satisfied the white noise assumptions, whereas the Grid 1.25×1.25 model did not. Although the MAPE value of 12.63% is slightly higher, it still indicates good predictive accuracy. Therefore, the spatial area-based model is considered the most appropriate for this study.

The final GSTAR model reveals diverse and location-specific fire dynamics across sub-districts. Jelai Hulu and Simpang Hulu are characterized by positive spatial spillover effects, where fire risk intensifies alongside neighboring activity, while Sungai Laur shows a negative spatial correlation, indicating reduced local risk when adjacent areas burn. Manis Mata operates as a spatially independent system, influenced solely by its own temporal behavior, as shown by the orange-highlighted (see equation 7). In Kapuas and Tumbang Titi, spatial relationships are negatively correlated, whereas Kendawangan exhibits positive spatial reinforcement. Overall, these patterns demonstrate that fire behavior varies markedly across regions, with the model effectively capturing each sub-district's unique spatial temporal interactions. The GSTAR(1;1) specification for the selected spatial area-based model employs the Queen Contiguity weight matrix, and the model equation can be expressed as follows:

$$
\begin{aligned}
\hat{Y}_t^{(1)} &= 0.113(Y_{t-1}^{(4)} + Y_{t-1}^{(5)} + Y_{t-1}^{(14)}) \\
\hat{Y}_t^{(2)} &= -0.062Y_{t-1}^{(2)} - 0.089(Y_{t-1}^{(6)} + Y_{t-1}^{(7)} + Y_{t-1}^{(10)} + Y_{t-1}^{(11)}) \\
\hat{Y}_t^{(3)} &= -0.537Y_{t-1}^{(3)} + 0.300(Y_{t-1}^{(4)} + Y_{t-1}^{(5)}) \\
\hat{Y}_t^{(4)} &= 0.071Y_{t-1}^{(4)} \\
\hat{Y}_t^{(12)} &= 0.048(Y_{t-1}^{(6)} + Y_{t-1}^{(13)}) \\
\hat{Y}_t^{(13)} &= -0.259(Y_{t-1}^{(9)} + Y_{t-1}^{(12)}) \\
\hat{Y}_t^{(14)} &= -0.973Y_{t-1}^{(14)} - 0.255(Y_{t-1}^{(1)} + Y_{t-1}^{(5)} + Y_{t-1}^{(8)})
\end{aligned}
\tag{7}
$$

To evaluate the performance of the selected spatial area-based GSTAR model, Figure 6 presents a visual comparison between the actual observed FRP values and the model's predictions for four representative sub-districts, illustrating the performance of the GSTAR(1;1) model by comparing the actual FRP values (green line) with in-sample predictions (blue line) and out-of-sample forecasts (yellow line). Overall, the in-sample predictions closely follow the observed FRP trends, capturing the main peaks during high-fire periods in August–September 2024 and July–August 2025. In Jelai Hulu (Figure 6a) and Kapuas (Figure 6b), the in-sample fits accurately replicate historical peaks, while the out-of-sample forecasts capture overall upward trends, albeit smoothing high-frequency fluctuations. In Kendawangan (Figure 6c), both in-sample and out-of-sample predictions closely match the observed patterns, including minor dips and subsequent rises. For Manis Mata (Figure 6d), the forecast successfully predicts the resurgence of fire activity following historical peaks. Despite minor discrepancies and a tendency to smooth sudden extreme spikes, the GSTAR model effectively captures temporal dynamics and periodic fire behavior in West Kalimantan.

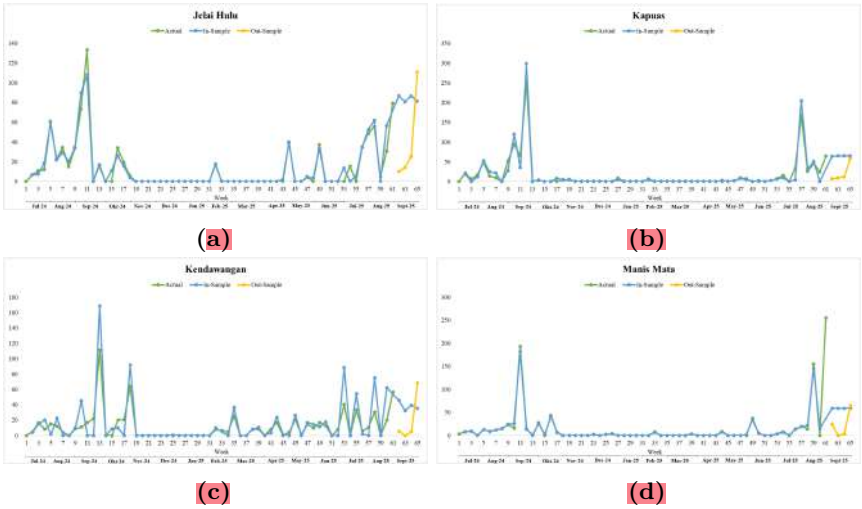

Figure 6: Comparison of Actual Data (green line), In-Sample Fit (blue line), and Out-of-Sample (yellow line) forecast for four representative sub-districts: (a) Jelai Hulu, (b) Kapuas, (c) Kendawangan, and (d) Manis Mata

Consequently, the forecasts produced by the model are subsequently used for spatial interpolation via the Ordinary Kriging method, as reported in Table 4.

Table 4: FRP Prediction for October. Yellow numbers represents locations (i)

Regencies	Subdistrict (i)	Week 1	Week 2	Week 3	Week 4	Illustration
Sanggau	Kapuas (2)	98.44	98.06	98.05	98.05	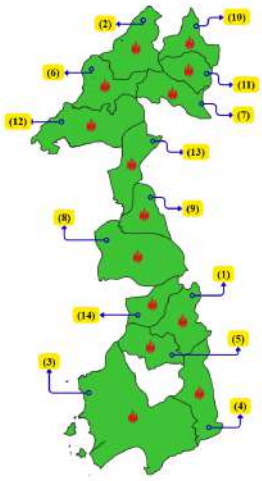
	Meliau (6)	58.15	58.15	58.15	58.15	
Sekadau	Sekadau Hilir (10)	111.17	111.17	111.17	111.17	
	Sekadau Hulu (11)	55.39	55.39	55.39	55.39	
	Nanga Taman (7)	80.15	80.15	80.15	80.15	
Ketapang	Jelai Hulu (1)	83.83	84.50	84.52	84.51	
	Nanga Tayap (8)	68.43	68.43	68.43	68.43	
	Sandai (9)	64.11	64.11	64.11	64.11	
	Kendawangan (3)	64.86	68.00	69.05	69.08	
	Sungai Laur (13)	131.65	131.59	131.59	131.59	
	Simpang Hulu (12)	133.26	133.19	133.19	133.19	
	Marau (5)	173.68	173.68	173.68	173.68	
	Manis Mata (4)	82.45	83.29	83.38	83.39	
	Tumbang Titi (14)	86.37	85.97	85.67	85.51	

Note: All FRP values are expressed in Megawatts (MW).

3.5 Interpolation of Fire Radiative Power (FRP)

Before performing spatial interpolation, the forecasted FRP data were first evaluated to ensure compliance with the Kriging model assumptions. A visual inspection confirmed mean stationarity, while the Kolmogorov–Smirnov test indicated non-normality. Consequently, a logarithmic transformation was applied, successfully normalizing the data for geostatistical analysis. Subsequently, the spatial dependence structure was modeled using a semivariogram. The model selection process was based on the lowest Root Mean Square Error (RMSE) values, representing the best fit and highest estimation accuracy. The comparison of semivariogram models for each week is presented in Figure 7, which shows that all variogram models yielded the same RMSE value of 0.08 across the four weeks.

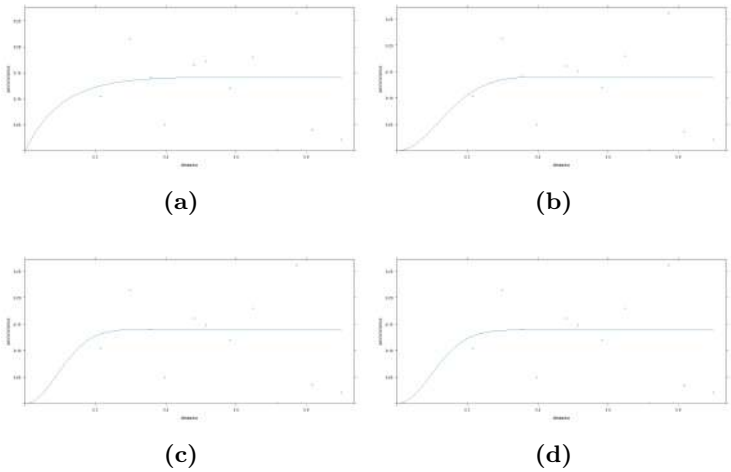

(a) **(b)**

(c) **(d)**

Figure 7: Semivariogram model plots with RMSE value of 0.08 for each week: (a) Week 1 Exponential model, (b) Week 2 Gaussian model, (c) Week 3 Gaussian model, and (d) Week 4 Gaussian model.

Therefore, spatial interpolation using Ordinary Kriging was conducted based on these models, and the resulting prediction maps are presented in Figure 8.

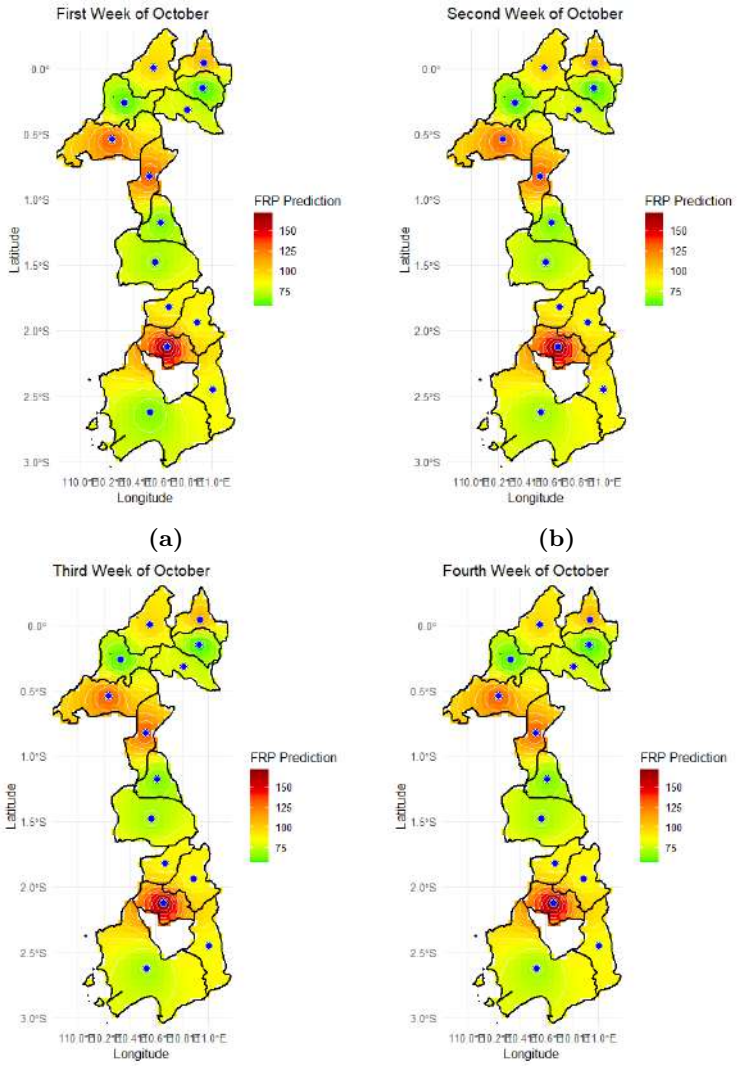

(a) **(b)**

(c) **(d)**

Figure 8: Interpolated FRP forecast maps for October 2025 (a) first week, (b) second week, (c) third week, and (d) fourth week

The interpolated forecast maps for October indicate that there are no significant changes in spatial fire intensity patterns from the first to the fourth week. Overall, the predicted FRP distribution remains relatively stable throughout the month. However, in the fourth week, a slight decrease in FRP levels is observed in the Nanga Tayap and Sandai sub-districts, as reflected by the color transition from light green to a darker green shade (see Figure 8d). This subtle shift suggests a localized reduction in fire potential, while the general spatial configuration of fire activity remains consistent across the observed period. A comparative illustration of the initial map, the GSTAR forecast map, and the Kriging interpolation results can be seen in Figure 9.

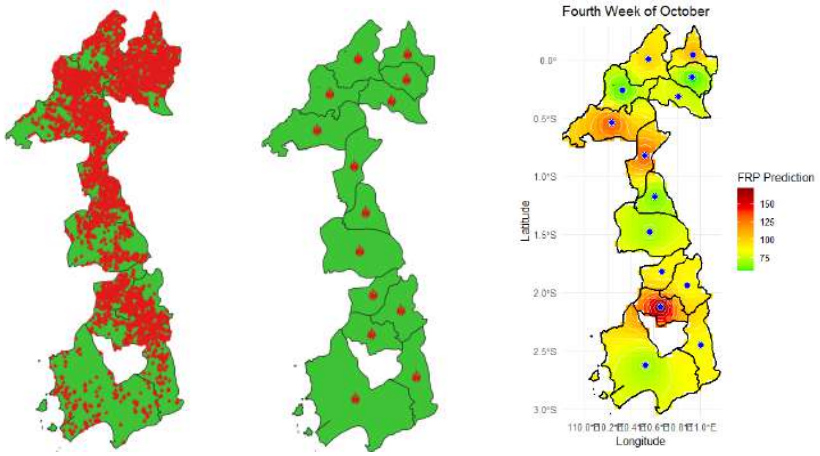

(a) **(b)** **(c)**

Figure 9: Comparison of spatial patterns: (a) actual FRP distribution, (b) Ilustration of GSTAR(1;1) model prediction, and (c) interpolated prediction using Ordinary Kriging.

4 Conclusion

This study successfully applied the GSTAR(1;1) and Ordinary Kriging methods to predict and visualize the spatial distribution of Fire Radiative Power (FRP) in Sanggau, Sekadau, and Ketapang Regencies. Using a spatial area-based approach, the model achieved optimal performance with a MAPE value of 12.63% and residuals that satisfied the white noise assumption, indicating good forecasting reliability. The prediction results for October 2025 show that the spatial fire intensity patterns remained relatively stable from the first to the fourth week. A minor decrease in FRP levels was observed in the Nanga Tayap and Sandai sub-districts during the final week, reflecting localized improvements in fire conditions. Overall, the integrated GSTAR–Kriging approach effectively captured both temporal and spatial patterns of FRP, making it a valuable tool for monitoring and managing fire risk in West Kalimantan. Furthermore, this integrated framework can support regional decision-making for wildfire management and environmental protection, providing a robust basis for preventive and mitigation strategies in fire-prone areas.

CRediT Authorship Contribution Statement

Gita Fitriyana: Conceptualization, Methodology, Writing-Original Draft. **Nurfitri Imro'ah:** Data Curation, Formal Analysis, Writing–Review & Editing. **Nur'ainul Miftahul Huda:** Data Curation, Formal Analysis, Writing–Review & Editing.

Declaration of Generative AI and AI-assisted technologies

No generative AI or AI-assisted technologies were used during the preparation of this manuscript.

Declaration of Competing Interest

The authors declare no competing interests.

Funding and Acknowledgments

This research received no external funding.

Data and Code Availability

The data and code supporting the findings of this study are available from the corresponding author upon reasonable request and subject to confidentiality agreements.

References

[1] C. Filizzola et al., "Fire characterization by using an original rst-based approach for fire radiative power (frp) computation," *Fire*, vol. 6, no. 2, p. 48, Jan. 2023. DOI: 10.3390/fire6020048. Available online.

[2] G. Fitriyana, N. Imro'ah, N. M. Huda, and Z. Zuleha, "Interpolation of Fire Radiative Power in West Kalimantan using Ordinary Kriging," *Jurnal Teori dan Aplikasi Matematika*, vol. 9, no. 4, pp. 1287–1300, 2025. DOI: https://doi.org/10.31764/jtam.v9i4.32643.

[3] E. B. Wiggins et al., "High temporal resolution satellite observations of fire radiative power reveal link between fire behavior and aerosol and gas emissions," *Geophysical Research Letters*, vol. 47, no. 23, Dec. 2020. DOI: 10.1029/2020gl090707. Available online.

[4] S. S. Kumar, J. Hult, J. Picotte, and B. Peterson, "Potential underestimation of satellite fire radiative power retrievals over gas flares and wildland fires," *Remote Sensing*, vol. 12, no. 2, p. 238, Jan. 2020. DOI: 10.3390/rs12020238. Available online.

[5] Z. Dong, C. Zheng, F. Zhao, G. Wang, Y. Tian, and H. Li, "A deep learning framework: Predicting fire radiative power from the combination of polar-orbiting and geostationary satellite data during wildfire spread," *IEEE Journal of Selected Topics in Applied Earth Observations and Remote Sensing*, vol. 17, pp. 10 827–10 841, 2024. DOI: 10.1109/jstars.2024.3403146. Available online.

[6] H. Pratiwi, N. Imro'ah, and N. M. Huda, "Forest fire analysis from perspective of spatial-temporal using gstar (p;λ_1, λ_2, ..., λ_p) model," *BAREKENG: Jurnal Ilmu Matematika dan Terapan*, vol. 19, no. 2, pp. 1379–1392, Apr. 2025. DOI: 10.30598/barekengvol19iss2pp1379-1392. Available online.

[7] Y. Supriya and T. R. Gadekallu, "Particle swarm-based federated learning approach for early detection of forest fires," *Sustainability*, vol. 15, no. 2, p. 964, Jan. 2023. DOI: 10.3390/su15020964. Available online.

[8] R. Alkhatib, W. Sahwan, A. Alkhatieb, and B. Schütt, "A brief review of machine learning algorithms in forest fires science," *Applied Sciences*, vol. 13, no. 14, p. 8275, Jul. 2023. DOI: 10.3390/app13148275. Available online.

[9] M. Y. Ayyash, N. M. Huda, and N. Imro'ah, "The gstar (1;1) modelling with three combination of the grid sizes and spatial weight matrix in forest fires cases," *JTAM (Jurnal Teori dan Aplikasi Matematika)*, vol. 9, no. 1, p. 134, Jan. 2025. DOI: 10.31764/jtam.v9i1.27543. Available online.

[10] X. Lu, M. Salehi, M. Haenggi, E. Hossain, and H. Jiang, "Stochastic geometry analysis of spatial-temporal performance in wireless networks: A tutorial," *IEEE Communications Surveys & Tutorials*, vol. 23, no. 4, pp. 2753–2801, 2021. DOI: 10.1109/comst.2021.3104581. Available online.

[11] S. Y. Chung, S. Venkatramanan, H. E. Elzain, S. Selvam, and M. Prasanna, "Supplement of missing data in groundwater-level variations of peak type using geostatistical methods," in *GIS and Geostatistical Techniques for Groundwater Science*. Elsevier, 2019, pp. 33–41. DOI: 10.1016/b978-0-12-815413-7.00004-3. Available online.

[12] U. Mukhaiyar, N. R. Dianti, E. S. Rezeki, and N. R. Richardo, "Prediksi risiko emisi karbon dioksida melalui pemodelan gstar kriging di wilayah asia," *Journal of Mathematics, Computations and Statistics*, vol. 7, no. 2, pp. 396–412, Oct. 2024. DOI: 10.35580/jmathcos.v7i2.4309. Available online.

[13] J. U. Devkota, "Statistical analysis of active fire remote sensing data: Examples from south asia," *Environmental Monitoring and Assessment*, vol. 193, no. 9, Aug. 2021. DOI: 10.1007/s10661-021-09354-x. Available online.

[14] N. M. Huda, N. Imro'ah, M. Y. Ayyash, and H. Pratiwi, "Forest fires in peatlands analyzed from various perspectives: Spatial, temporal, and spatial-temporal," *JTAM (Jurnal Teori dan Aplikasi Matematika)*, vol. 9, no. 2, p. 482, Apr. 2025. DOI: 10.31764/jtam.v9i2.28884. Available online.

[15] F. Hestuningtias and M. H. S. Kurniawan, "The implementation of the generalized space-time autoregressive (gstar) model for inflation prediction," *Enthusiastic: International Journal of Applied Statistics and Data Science*, pp. 176–188, Oct. 2023. DOI: 10.20885/enthusiastic.vol3.iss2.art5. Available online.

[16] H. Pratiwi, N. Imro'ah, N. M. Huda, and M. Y. Ayyash, "Comparison of weight matrix in hotspot modeling in west kalimantan using the gstar method," *Jurnal Matematika UNAND*, vol. 14, no. 1, pp. 31–45, Jan. 2025. DOI: 10.25077/jmua.14.1.31-45.2025. Available online.

[17] Yundari, U. S. Pasaribu, U. Mukhaiyar, and M. N. Heriawan, "Spatial weight determination of gstar(1;1) model by using kernel function," *Journal of Physics: Conference Series*, vol. 1028, p. 012 223, Jun. 2018. DOI: 10.1088/1742-6596/1028/1/012223. Available online.

[18] N. M. Huda and N. Imro'ah, "Determination of the best weight matrix for the generalized space time autoregressive (gstar) model in the covid-19 case on java island, indonesia," *Spatial Statistics*, vol. 54, p. 100 734, Apr. 2023. DOI: 10.1016/j.spasta.2023.100734. Available online.

[19] Y. Yundari, U. S. Pasaribu, and U. Mukhaiyar, "Error assumptions on generalized star model," *Journal of Mathematical and Fundamental Sciences*, vol. 49, no. 2, p. 136, Oct. 2017. DOI: 10.5614/j.math.fund.sci.2017.49.2.4. Available online.

[20] P. Kumar, B. Rao, A. Burman, S. Kumar, and P. Samui, "Spatial variation of permeability and consolidation behaviors of soil using ordinary kriging method," *Groundwater for Sustainable Development*, vol. 20, p. 100 856, Feb. 2023. DOI: 10.1016/j.gsd.2022.100856. Available online.

[21] C. Wu, *Interpolation: Kriging*, Mar. 2017. DOI: 10.1002/9781118786352.wbieg0996. Available online.

[22] J. Böhner and B. Bechtel, "Gis in climatology and meteorology," in *Comprehensive Geographic Information Systems*. Elsevier, 2018, pp. 196–235. DOI: 10.1016/b978-0-12-409548-9.09633-0. Available online.

[23] N. N. Rohma, "Estimation of ordinary kriging method with jackknife technique on rainfall data in malang raya," *International Journal on Information and Communication Technology (IJoICT)*, vol. 8, no. 2, pp. 22–39, Dec. 2022. DOI: 10.21108/ijoict.v8i2.678. Available online.

[24] M. Khan, M. M. A. Almazah, A. EIlahi, R. Niaz, A. Y. Al-Rezami, and B. Zaman, "Spatial interpolation of water quality index based on ordinary kriging and universal kriging," *Geomatics, Natural Hazards and Risk*, vol. 14, no. 1, Mar. 2023. DOI: 10.1080/19475705.2023.2190853. Available online.

[25] T. Gia Pham, M. Kappas, C. Van Huynh, and L. Hoang Khanh Nguyen, "Application of ordinary kriging and regression kriging method for soil properties mapping in hilly region of central vietnam," *ISPRS International Journal of Geo-Information*, vol. 8, no. 3, p. 147, Mar. 2019. DOI: 10.3390/ijgi8030147. Available online.

[26] M. Li, S. Shen, V. Barzegar, M. Sadoughi, C. Hu, and S. Laflamme, "Kriging-based reliability analysis considering predictive uncertainty reduction," *Structural and Multidisciplinary Optimization*, vol. 63, no. 6, pp. 2721–2737, Jan. 2021. DOI: 10.1007/s00158-020-02831-w. Available online.

[27] A. Setiyoko, T. Basaruddin, and A. M. Arymurthy, "Minimax approach for semivariogram fitting in ordinary kriging," *IEEE Access*, vol. 8, pp. 82 054–82 065, 2020. DOI: 10.1109/access.2020.2991428. Available online.

[28] H. Xia, S. Zha, J. Huang, and J. Liu, "Radio environment map construction by adaptive ordinary kriging algorithm based on affinity propagation clustering," *International Journal of Distributed Sensor Networks*, vol. 16, no. 5, p. 155 014 772 092 248, May 2020. DOI: 10.1177/1550147720922484. Available online.

[29] A. H. Wong and T. J. Kwon, "Development and evaluation of geostatistical methods for estimating weather related collisions: A large-scale case study," *Transportation Research Record: Journal of the Transportation Research Board*, vol. 2675, no. 11, pp. 828–840, Jul. 2021. DOI: 10.1177/03611981211020008. Available online.

[30] N. S. V. Studio. "Active fires as observed by viirs, 2020." Accessed on October 31, 2025, NASA Goddard Space Flight Center. Available online.

[31] U. Mukhaiyar, "The goodness of generalized star in spatial dependency observations modeling," in *AIP Conference Proceedings*, AIP Publishing LLC, 2015. DOI: 10.1063/1.4936436. Available online.

[32] A. Roza, E. S. Violita, and S. Aktivani, "Study of inflation using stationary test with augmented dickey fuller & phillips-peron unit root test (case in bukittinggi city inflation for 2014-2019)," *EKSAKTA: Berkala Ilmiah Bidang MIPA*, vol. 23, no. 02, pp. 106–116, Jun. 2022. DOI: 10.24036/eksakta/vol23-iss02/303. Available online.